Research Square

Preprints are preliminary reports that have not undergone peer review.
They should not be considered conclusive, used to inform clinical practice,
or referenced by the media as validated information.

One-step synthesis of anhydrous $Mg(NO_3)_2$-$NaNO_3$-KNO_3 molten salt for high-temperature thermal energy storage

Hongtao Zhang

zhanght21@lzu.edu.cn

Qinghai Normal University

Xin Xu

Qinghai Normal University

Huaiyou Wang

Qinghai Institute of Salt Lakes

Yongfeng Gao

University of Alberta

Wei Chen

Qinghai Normal University

Min Wang

University of Chinese Academy of Sciences

Research Article

Keywords: Molten nitrate salt, Thermal stability, Dehydration, Thermal energy storage, TG-DSC

Posted Date: July 22nd, 2026

DOI: https://doi.org/10.21203/rs.3.rs-10350474/v1

License: This work is licensed under a Creative Commons Attribution 4.0 International License.
Read Full License

Additional Declarations: No competing interests reported.

Abstract

Molten nitrate salts are among the most promising heat transfer and storage media for concentrating solar power applications. In this study, a series of $Mg(NO_3)_3$-$NaNO_3$-KNO_3 (MNK) ternary molten salts were fabricated via a one-step synthesis strategy involving the dehydration of $Mg(NO_3)_2·6H_2O$. The thermal decomposition behavior, phase transition characteristics, and cycling durability of the as-prepared samples were systematically investigated by thermogravimetry-differential scanning calorimetry (TG-DSC) coupled with X-ray diffraction (XRD). Compared with the original hydrated MNK salt, the anhydrous MNK composite exhibited a significant enhancement in thermal stability. The onset decomposition temperature was elevated from 404.1 to 457.6°C, extending the upper operational limit to 450°C. Concurrently, the endothermic melting peak shifted from 157.5 to 148.2°C, accompanied by an increase in the latent heat of fusion from 66.61 to 88.71 $J·g^{-1}$. TG analysis revealed a reduction in the mass loss rate during long-term thermal exposure, indicating suppressed deterioration. Furthermore, XRD patterns confirmed the structural integrity of the anhydrous MNK salt after thermal cycling, demonstrating improved phase stability. Owing to its favorable thermophysical properties and scalable preparation, this anhydrous MNK ternary molten salt represents a viable candidate for high-temperature thermal energy storage.

1. Introduction

Thermal energy storage (TES) integrated with concentrating solar power (CSP) has emerged as a pivotal technology for addressing the intermittency of renewable energy and reducing reliance on fossil fuels [1, 2]. Molten nitrate salts are widely recognized as the state-of-the-art heat transfer and storage media due to their relatively low vapor pressure, high sensible heat capacity, and moderate cost [3–16]. However, the commercial Solar Salt (60 wt% $NaNO_3$–40 wt% KNO_3) suffers from a relatively high melting point (~ 220°C) and a limited upper operational temperature (< 400°C), primarily owing to the thermal decomposition of nitrate anions [17–28]. These limitations restrict the operational temperature window and overall thermal efficiency of CSP plants. Consequently, considerable efforts have been devoted to developing modified nitrate-based multicomponent systems, particularly through the incorporation of alkaline earth metal nitrates such as $Mg(NO_3)_2$ [29–33].

Building upon these modification strategies, the incorporation of magnesium nitrate to lower the phase change temperature of conventional binary nitrates has been extensively explored. Zhong et al. [34, 35] demonstrated that the addition of $Mg(NO_3)_2$ to the Solar Salt matrix effectively reduced the melting point and viscosity while enhancing the thermal conductivity of the ternary system. Subsequent studies have further focused on optimizing the composition; for instance, Han et al. [36] developed molten salt-based nanofluids via doping strategies, and Zhong et al. [37, 38] established a thermodynamic model to predict the eutectic composition of the $Mg(NO_3)_2$-$NaNO_3$-KNO_3 system, which was later validated by DSC measurements. Despite these advances, the utilization of $Mg(NO_3)_2·6H_2O$ as a raw material introduces significant challenges. The presence of crystal water tends to induce hydrolysis during the melting

process, leading to the formation of basic nitrates (e.g., $Mg(OH)(NO_3)_2$) and the release of corrosive NO_x gases upon thermal cycling [39–43]. Consequently, the thermal stability deteriorates, and the operational temperature window narrows due to the premature decomposition of hydrated salt. Although several dehydration protocols have been proposed, achieving complete dehydration without compromising the eutectic structure remains a technical bottleneck for high-temperature TES applications.

Motivated by these unresolved stability issues, this work develops a facile one-step synthesis strategy to fabricate anhydrous $Mg(NO_3)_2$-$NaNO_3$-KNO_3 (MNK) ternary molten salts via the controlled dehydration of $Mg(NO_3)_2·6H_2O$. Particular attention was paid to the thermal decomposition kinetics and phase evolution during the dehydration process, aiming to suppress hydrolysis and eliminate residual moisture. The thermophysical properties, including the melting behavior, latent heat, and specific heat capacity, were systematically characterized by differential scanning calorimetry (DSC) and thermogravimetric analysis (TGA). Furthermore, the thermal cycling durability and structural stability of the optimized MNK composite were evaluated under simulated operational conditions. It is demonstrated that the tailored dehydration process not only lowers the melting point but also significantly elevates the onset decomposition temperature, thereby extending the operational temperature window. This study provides a scalable route for designing high-performance nitrate-based thermal energy storage materials with enhanced thermal stability.

2. Experiment

2.1. Materials

A series of $Mg(NO_3)_2$-$NaNO_3$-KNO_3(MNK) ternary molten salts were synthesized by mixing predetermined amounts of sodium nitrate (> 99% purity), potassium nitrate (purity ≥ 99.0%), and magnesium nitrate hexahydrate (98%) purchased from Aladdin Chemical Co., Ltd.Preparation of MNK composites

2.2. Preparation of MNK composites

2.2.1 Dehydration process of $Mg(NO_3)_2·6H_2O$

Ten grams of $Mg(NO_3)_2·6H_2O$ was placed in a custom-designed corundum crucible (No. 2) and subjected to thermal treatment in a muffle furnace under a gas flow rate of 100 $mL·min^{-1}$. Three sets of experiments, designated as A, B, and C, were conducted according to the parameters listed in Table 1. Subsequently, the crucible was rapidly transferred into a glove box and cooled to room temperature.

Table 1
Experimental parameters for samples A, B, and C.

Tests	A/B			C
	Run 1	Run 2	Run 3	Run 1
atmosphere	air	vacuum	vacuum	air
Initial Temperature (℃)	25	150	250	25
Heating Rate (℃·min^{-1})	5	5	5	5
Target Temperature (℃)	150	250	300	300
Holding Time (min)	60	120–180	120	360

A vacuum environment was maintained during thermal treatment.

2.2.2. Preparation of MNK composites

Sodium nitrate and potassium nitrate were purified following previously reported procedures [44, 45]. $NaNO_3$ and KNO_3 were weighed according to the target ratio of 17.77 wt% $Mg(NO_3)_2$, 15.28 wt% $NaNO_3$, and 35.97 wt% KNO_3 in a glove box and thoroughly mixed in corundum crucible No.1. Subsequently, 10.0 g of $Mg(NO_3)_2{\cdot}6H_2O$ was added to the specially designed corundum crucible No. 2. The two crucibles were then assembled as illustrated in Fig. 1. Following the dehydration protocol described in Section 2.2.1, a staged heating program was implemented to dehydrate and melt-blend the mixture to form the eutectic ternary nitrate molten salt. The mixture was heated to approximately 50 K above the predicted melting temperature and held for 2–3 h. After complete homogenization, the salt mixture was cooled to ambient temperature. This procedure was repeated 3–4 times to ensure a homogeneous eutectic mixture. The entire preparation process was conducted inside a glove box was purged with high-purity argon to prevent moisture absorption.

2.3. Characterization

The specific heat capacity (C_p) and melting point of all samples were measured using thermogravimetry–differential scanning calorimetry (TG-DSC, PerkinElmer, USA). X-ray diffraction (XRD, D8 Advance, Bruker, Germany) with Cu Kα radiation (λ = 1.5405 Å) was performed to identify the crystalline phases of the samples after melt-blending. The concentrations of impurity ions were determined via ion chromatography (ICAP 6500 DUO, Thermo Fisher Scientific, USA). Raman spectra were acquired using a laser confocal Raman spectrometer (Renishaw in Via, UK).

For thermal cycling tests, the molten salts were placed in a muffle furnace and completely melted at target temperatures (250, 300, 350, 400, 450, and 500°C) at a heating rate of 5°C·min^{-1}. The samples were held at the target temperature for 27 h and then naturally cooled to room temperature. The masses

of the cooled solids were weighed using an analytical balance and recorded. This procedure was repeated ten times to generate mass loss versus time curves at different temperatures.

3. Results and discussion

3.1 TG-DSC analysis

Figure 2 shows the TG and DSC curves of $Mg(NO_3)_2·6H_2O$ thermal decomposition under a nitrogen atmosphere at a heating rate of 10 ℃·min^{-1}. Three distinct peaks observed in the DTG curve indicate that the thermal decomposition of $Mg(NO_3)_2·6H_2O$ is a multi-step reaction involving three mass loss stages. The broad endothermic peak at 110.35°C corresponds to the first mass loss stage (30.41%), associated with the initial dehydration. The second stage exhibits a mass loss of 11.25% with a DTG peak at 290.75°C, followed by a sharp third mass loss of 42.55% peaking at 444.45°C. The total mass loss of 84.46% closely matches the theoretical value of 84.28% for the conversion of $Mg(NO_3)_2·6H_2O$ to MgO, confirming the completion of thermal decomposition. The endothermic nature of these processes is evident in the DSC curve, suggesting that the dehydration and decomposition reactions are thermally activated.

3.2 XRD and Raman analysis

Figure 3 shows the XRD patterns of the samples during the hydrolysis and dehydration of $Mg(NO_3)_2·6H_2O$. At room temperature, the phase is identified as $Mg(NO_3)_2·6H_2O$. Upon heating to 300℃ and holding for 6 h in air, diffraction peaks corresponding to $Mg(NO_3)_2·2H_2O$, $Mg(OH)(NO_3)_2$, and $Mg(NO_3)_2$ emerge, indicating the formation of intermediate phases. In contrast, samples A and B, prepared via the staged temperature programming outlined in Table 1, exhibited distinct phase evolution. After heating to 300℃ and dehydrating for 2 h, only the diffraction peaks of $Mg(NO_3)_2·2H_2O$ were identified. After 3 h, the peaks of rhombohedral $Mg(NO_3)_2$ appeared, signifying the transformation into the anhydrous phase. From 2 h to 3 h, the rhombohedral $Mg(NO_3)_2$ transitioned into a more thermodynamically stable cubic structure [47].

Raman spectroscopy was further employed to characterize the structural evolution during the dehydration process (Fig. 4). The spectrum of the sample dehydrated at 300°C for 30 min exhibits characteristic peaks at 1061.31 cm^{-1} and 1097.78 cm^{-1}, corresponding to $Mg(NO_3)_2·6H_2O$ and $Mg(NO_3)_2·2H_2O$, respectively. After extending the dehydration time to 2 h at 300°C, the intensity of the peak at 1061.31 cm^{-1} was significantly suppressed, while the peak at 1097.78 cm^{-1} remained unchanged, confirming the predominant existence of $Mg(NO_3)_2·2H_2O$. Notably, after 3 h of dehydration at 300°C, the spectral features evolved distinctly: characteristic peaks appeared simultaneously at 1097.78 cm^{-1} and 1101.14 cm^{-1}, demonstrating the coexistence of $Mg(NO_3)_2·2H_2O$ and anhydrous $Mg(NO_3)_2$. The absence of the 1061.31 cm^{-1} peak, coupled with the persistence of the 1097.78 cm^{-1} and 1101.14 cm^{-1} peaks, indicates that the product after 3 h comprises $Mg(NO_3)_2·2H_2O$ and $Mg(NO_3)_2$,

which corroborates the XRD results. These findings confirm that the intermediate $Mg(NO_3)_2·2H_2O$ phase is stable within this temperature-time window, providing a critical basis for optimizing the subsequent calcination parameters of the MNK ternary molten salt.

3.3 Microstructure and basic thermophysical properties

The surface morphology and elemental distribution of the dehydrated MNK sample (Sample A) were characterized by SEM and EDX mapping (Fig. 5a–f). The nitrate matrix exhibited a flat surface with uniformly distributed angular grains. EDX mapping confirms the homogeneous distribution of Na, K, Mg, O, and N throughout the composite (Fig. 5b-f). The coexistence of Mg, Na, and K elements verifies the formation of a homogeneous eutectic mixture. As shown in Fig. 5g, the XRD pattern of the dehydrated sample (A) is identical to that of the pristine MNK salt (Sample C), indicating that the dehydration process does not alter the crystalline phase composition.

TG analysis reveals that the dehydrated MNK ternary molten salt begins to decompose at 457.6°C, with the maximum decomposition rate occurring at 546.3°C. In contrast, the non-dehydrated sample exhibited a mass loss of 4.69% upon heating to 150°C due to the evaporation of moisture trapped in the pores of the hydrated salt. The onset decomposition temperature of the dehydrated MNK salt increased by 53.5°C compared to the original MNK salt. The DSC curve of the dehydrated sample exhibits a single endothermic peak at 148.2°C, corresponding to a latent heat of fusion of 88.71 $J·g^{-1}$. Compared with the non-dehydrated MNK salt, this represents a decrease of 9.3°C in the melting point and an increase of 22.1 $J·g^{-1}$ in the latent heat. These results demonstrate that the tailored dehydration process effectively elevates the thermal stability and broadens the operational temperature window.

3.4 Thermal storage performance

The phase-change heat storage performance is a critical criterion for evaluating the applicability of molten salts. As summarized in Table 2, the melting point of the dehydrated MNK ternary molten salt is 147.90°C, representing a 5.1% reduction compared to the non-dehydrated sample (155.85°C). The phase change enthalpy and decomposition temperature increased by 12.1% and 6.35% to 84.38 $J·g^{-1}$ and 451.08°C, respectively, which is consistent with previous thermodynamic predictions [37, 42].

Table.2 The TG-DSC data and Specific heat capacities of the A, C sample.

	Average							
	Tm (℃)	**ΔHm (J·g-1)**	**Tonset (℃)**	**ΔT (℃)**	**1st**	**2nd**	**3rd**	**Cp (J·g-1·K-1)**
A	147.90 ± 1.30	84.38 ± 1.01	451.08 ± 1.29	303.18 ± 0.01	1.578	1.571	1.567	1.572 ± 0.01
C	155.85 ± 1.45	75.25 ± 1.76	400.05 ± 2.13	244.19 ± 0.68	1.214	1.213	1.205	1.211 ± 0.01

The liquid specific heat capacity (C_p), measured at 300°C, increased from 1.211 $J·(g·K)^{-1}$ for the non-dehydrated salt to 1.572 $J·(g·K)^{-1}$ for the dehydrated salt, an improvement of 13.1%. This enhancement is attributed to the increased interfacial thermal resistance resulting from the porous structure formed during dehydration (Fig. 5a), which promotes phonon scattering and enhances sensible heat storage.

Cyclic stability was evaluated between 25 and 300°C through 720 h of thermal cycling. Even after 30 cycles, the dehydrated MNK salt maintained its initial melting point, phase change enthalpy, and decomposition temperature with only marginal deviations. Specifically, the decomposition temperature remained stable at 451.08°C, which was significantly higher than that of the non-dehydrated control. Notably, the non-dehydrated sample exhibited a sharp decline in melting point after 550 h of cycling due to the onset of decomposition. The specific heat capacity of the dehydrated sample also remained stable throughout the 720 h test. These findings confirm that the dehydration strategy effectively suppresses hydrolysis and significantly improves the long-term thermal stability of MNK ternary molten salts.

3.5Thermal stability

The decomposition profiles of the molten salts during 300 h of cyclic testing are presented in Fig. 7a and 7b. The dehydrated MNK molten salt exhibited mass losses of 0.055%, 1.04%, and 2.01% at 350, 400, and 450°C, respectively, which were significantly lower than those of the non-dehydrated MNK salt (2.29%, 3.51% and 8.61%, respectively; Fig. 7b). These results indicate that the dehydrated MNK ternary molten salt is more thermally stable below 450°C (defined as the temperature range where mass loss remains below 3%). The substantial mass loss (8.61%) observed in the non-dehydrated sample at 450°C is attributed to the evaporation of moisture trapped within the salt matrix and the decomposition of residual $Mg(NO_3)_2·2H_2O$. Above 500°C, the non-dehydrated sample suffered a severe mass loss of 17.71%, indicating the near-complete decomposition of the hydrated nitrate into MgO and basic nitrates, such as $Mg(OH)(NO_{3)}$.

The concentrations of NO_2^- and $Mg(OH)(NO_3)$ after ten thermal cycles were analyzed via ion chromatography to further elucidate the hydrolysis behavior (Fig. 7c and 7d). In the non-dehydrated MNK molten salt, NO_2^- was detected at temperatures above 400°C, coinciding with the onset of non-eutectic nitrate decomposition. In contrast, NO_2^- was undetectable in the dehydrated MNK molten salt below 450°C, and its concentration remained negligible even above this threshold. Correspondingly, $Mg(OH)(NO_3)$ identified as the primary hydrolytic product was detected in the non-dehydrated sample across all tested temperatures (250–500°C), with a maximum content of 10.01 wt% at 500°C. Crucially, $Mg(OH)(NO_3)$ was absent in the dehydrated MNK molten salt. These findings confirm that the optimized dehydration process effectively suppresses hydrolysis and stabilizes the nitrate matrix, thereby extending the operational temperature window of the MNK ternary molten salt.

4. Conclusions

A novel anhydrous $Mg(NO_3)_2$-$NaNO_3$-KNO_3 (MNK) ternary molten salt was successfully fabricated via a one-step synthesis strategy involving controlled dehydration. The main conclusions are as follows:

1. Enhanced Thermal Stability: The optimized dehydration process effectively suppressed hydrolysis, elevating the upper operational limit from 400 to 450°C and significantly improving long-term cycling durability.
2. Optimized Thermophysical Properties: The tailored dehydration lowered the melting point from 157.5 to 148.2°C while increasing the latent heat of fusion from 66.6 to 88.71 $J{\cdot}g^{-1}$, broadening the operational temperature window.
3. Structural Integrity: After 720 h of thermal cycling, the dehydrated MNK salt maintained compositional stability and a high latent heat of 84.38 $J{\cdot}g^{-1}$, attributed to the reduction of impurity levels and the elimination of residual moisture.

This work provides a feasible and scalable route for manufacturing high-performance nitrate-based thermal energy storage materials, demonstrating great potential for concentrating solar power applications.

Declarations

CRediT authorship contribution statement

Hongtao Zhang and Xin Xu: Writing-original draft, Formal analysis, Data curation, Writing-review & editing, Methodology, Funding acquisition. Huaiyou Wang: Formal analysis, Data curation. Yongfeng Gao: Writing – review & editing, Formal analysis. Wei Chen: Formal analysis, Data curation. Min Wang: Data curation.

Declaration of competing interest

The authors declare that they have no known competing financial interests or personal relationships that could have appeared to influence the work reported in this paper.

Author Contribution

Z and X: Writing-original draft, Formal analysis, Data curation, Writing-review & editing, Methodology, Funding acquisition. W: Formal analysis, Data curation. G: Writing – review & editing, Formal analysis.C: Formal analysis, Data curation. W: Data curation.

Acknowledgement

This work was supported by the Young and Middle-aged Fund Project of Qinghai Normal University (grant number: KJQN2022003) and the National college students' innovation and entrepreneurship

training program of China (grant number: 202210746007).

Data availability

The raw data required to reproduce these findings are available upon reasonable request to the corresponding author.

References

1. Bonk A, Sa S, Uranga N, Hernaiz M, Bauer T. Advanced heat transfer fluids for direct molten salt line-focusing CSP plants. Prog Energy Combust Sci 2018; 67: 69–87. https://doi.org/10.1016/j.pecs.2018.02.002.
2. Maia CB, Neumann LR, de Andrade Oliveira G, Igor Marques L, Walczak MM, Brito PP. A comprehensive review of solar tower CSP systems using TES and molten salts. Int J Ambient Energy 2023; 28: 2185814. https://doi.org/10.1080/01430750.2023.2185814.
3. Du BC, Guo YF, Xu C, Huang LJ, Li XF, Lei YG. Dynamic creep and stress performances of the packed-bed thermal energy storage tank with molten salt EPCM particles. Appl Therm Eng 2023; 225: 120247. https://doi.org/10.1016/j.applthermaleng.2023.120247.
4. Khan MI, Asfand F, Al-Ghamdi SG. Progress in research and development of phase change materials for thermal energy storage in concentrated solar power. Appl Therm Eng 2022; 217: 119546. https://doi.org/10.1016/j.applthermaleng.2022.119546.
5. Chavan S, Rudrapati R, Manickam S. Advances in thermal energy storage systems-methods and applications. Alex Eng J 2022; 61: 5455–5463. https://doi.org/10.1016/j.aej.2021.11.003.
6. Zhang H, Baeyens J, Degrève J, Cacères G. Thermal energy storage: recent developments and practical aspects. Prog Energy Combust Sci 2016; 53: 1–40. https://doi.org/10.1016/j.pecs.2015.10.003.
7. Lizana J, Chacartegui R, Barrios-Padura A, Valverde JM. Advances in thermal energy storage materials and their applications towards zero energy buildings: A critical review. Appl Energy 2017; 203: 219–239. https://doi.org/10.1016/j.apenergy.2017.06.008.
8. Ahmed SF, Khalid M, Rashmi W, Chan A, Shahbaz K. Recent progress in solar thermal energy storage using nanomaterials. Renew Sust Energ Rev 2017; 67: 450–460. https://doi.org/10.1016/j.rser.2016.09.034.
9. Sau S, Corsaro N, Crescenzi T, D'Ottavi C, Liberatore R, Licoccia S, Russo V, Tarquini P, Tizzoni AC. Techno-economic comparison between CSP plants presenting two different heat transfer fluids. Appl Energy 2016; 168: 96–109. https://doi.org/10.1016/j.apenergy.2016.01.066.
10. Sang LX, Lv XY, Wang YC, Huang J, Wu YT. Investigation of KNO_2-KNO_3-K_2CO_3 mixed molten salts with higher working temperature for supercritical CO_2 concentrated solar power application. J Energy Storage 2023; 61: 106724. https://doi.org/10.1016/j.est.2023.106724.

11. Zhao D, Yan LM, Jiang TJ, Peng SM, Yue BH. On the viscosity of molten salts and molten salt mixtures and its temperature dependence. J Energy Storage 2023; 61: 106707. https://doi.org/10.1016/j.est.2023.106707.
12. Nunes VM, Queiro's CS, Lourenco MJ, Santos FV, Nieto de Castro CA. Molten salts as engineering fluids-A review Part I. Molten alkali nitrates. Appl Energy 2016; 183: 603–611. https://doi.org/10.1016/j.apenergy.2016.09.003.
13. Caceres G, Anrique N, Girard A, Degreve J, Baeyens J, Zhang HL. Performance of molten salt solar power towers in Chile. J Renew Sustain Energy 2013; 5: 053142. https://doi.org/10.1063/1.4826883.
14. Akanda MAM, Shin D. A synthesis parameter of molten salt nanofluids for solar thermal energy storage applications. J Energy Storage 2023; 60: 106608. https://doi.org/10.1016/j.est.2023.106608.
15. Xu HX, Wang Y, Li N, Ling CJ, Liu Q, Tang ZF. Corrosion performance of 316 stainless steel and nodular cast iron 600-3 in molten $Ca(NO_3)_2$-$NaNO_3$-KNO_3 salt. J Energy Storage 2023; 57: 106231. https://doi.org/10.1016/j.est.2022.106231.
16. Vaka M, Walvekar R, Khalid M, Jagadish P. Low-melting-temperature binary molten nitrate salt mixtures for solar energy storage. J Therm Anal Calorim 2020; 141: 2657–2664. https://doi.org/10.1007/s10973-020-09683-y.
17. Chen MM, Shen YS, Zhu SM, Li PW. Digital phase diagram and thermophysical properties of KNO_3-$NaNO_3$-$Ca(NO_3)_2$ ternary system for solar energy storage. Vacuum 2017; 145: 225–233. https://doi.org/10.1016/j.vacuum.2017.09.003.
18. Zhang XP, Lu YW, Yu Q, Wu YT, Zhang CC. Study on preparation and thermophysical characteristics of molten salt nanocomposite by microwave method. Sol Energy Mater Sol Cells 2021; 220: 110846. https://doi.org/10.1016/j.solmat.2020.110846.
19. Giaconia A, Balog I, Caputo G. Hybridization of CSP Plants: Characterization of a Molten Salt Heater for Binary and Ternary Nitrate Salt Mixtures Fueled with Gas/Biogas Heaters. Energies 2021; 14: 7652. https://doi.org/10.3390/en14227652.
20. Giaconia A, Iaquaniello G, Metwally AA, Caputo G, Balog I. Experimental demonstration and analysis of a CSP plant with molten salt heat transfer fluid in parabolic troughs. Sol Energy 2020; 211: 622–632. https://doi.org/10.1016/j.solener.2020.09.091.
21. Bell S, Steinberg T, Will G. Corrosion mechanisms in molten salt thermal energy storage for concentrating solar power. Renew Sust Energ Rev 2019; 114: 109328. https://doi.org/10.1016/j.rser.2019.109328.
22. Kasedde H, Namagambe A, Lwanyaga JD, Kirabira JB, Okumu D. Numerical modelling of a solar salt pan for improved salt production at Lake Katwe, Uganda. Case Stud Therm Eng 2022; 42: 102592. https://doi.org/10.1016/j.csite.2022.102592.
23. Yan C, Liang JF, Zhong XB, Li C, Chen DK, Wang ZW, Li SX, Xu JF, Wang H, Li YF, Zhan YG, Liu HT. BN white graphene well-dispersed solar salt nanofluids with significant improved thermal properties for

concentrated solar power plants. Sol Energy Mater Sol Cells 2022; 245: 111875. https://doi.org/10.1016/j.solmat.2022.111875.

24. Mao R, Yang QR, Li ZY, Yan CX, He ZY, Zhang YQ. Analysis of scale and frame interface effects on the solidification properties of solar salt in mesopores. Sol Energy Mater Sol Cells 2022; 247: 111949. https://doi.org/10.1016/j.solmat.2022.111949.
25. He ZY, Yang QR, Li ZY, Mao R, Yan CX. Effect of the mesoporous size, structure and surface on the melting and heat transport properties of solar salt. Sol Energy Mater Sol Cells 2022; 248: 111978. https://doi.org/10.1016/j.solmat.2022.111978.
26. Kondaiah P, Pitchumani R. Fractal coatings of Ni and NiYSZ for high-temperature corrosion mitigation in solar salt. Corros Sci 2022; 201: 110283. https://doi.org/10.1016/j.corsci.2022.110283.
27. Saranprabhu MK, Suganthi KS, Rajan KS. Assessment of the Effects of Copper Oxide Nanoparticles Addition to Solar Salt: Implications for Thermal Energy Storage. Int J Thermophys 2022; 43: 162. https://doi.org/10.1007/s10765-022-03085-y.
28. Sun Z, Su L, Gao XY, Lu GM, Song XF, Yu JG. Influences of impurity Cl on the thermal performance of solar salt for thermal energy storage. Sol Energy 2021; 216: 90–95. https://doi.org/10.1016/j.solener.2020.12.057.
29. Zhang CC, Han Y, Wu YT, Lu YW. Comparative study on high temperature thermal stability of quaternary nitrate-nitrite mixed salt and Solar salt. Sol Energy Mater Sol Cells 2021; 230: 111197. https://doi.org/10.1016/j.solmat.2021.111197.
30. Han Y, Zhang CC, Wu YT, Lu YW. Investigation on thermal performance of quaternary nitrate-nitrite mixed salt and solar salt under thermal shock condition. Renew Energy 2021; 175: 1041–1051. https://doi.org/10.1016/j.renene.2021.05.002.
31. Glazov VI, Dukhanin GP, Losev VA. Partial Saturated Vapor Pressure of Sodium Nitrite Over the System $NaNO_2$-KNO_3. Russ J Appl Chem 2002; 75: 891–893. https://doi.org/10.1023/A:1020364008208.
32. Coccia G, Nicola GD, Tomassetti S, Pierantozzi M, Chieruzzi M, Torre L. Experimental validation of a high-temperature solar box cooker with a solarsalt-based thermal storage unit. Sol Energy 2018; 170: 1016–1025. https://doi.org/10.1016/j.solener.2018.06.021.
33. Naresh G, Rajasekhar A, Bharali J, Ramesh K. Homogeneous molten salt formulations as thermal energy storage media and heat transfer fluid. J Energy Storage 2022; 50: 104200. https://doi.org/10.1016/j.est.2022.104200.
34. Zhong Y, Yang HJ, Wang M. Thermodynamic evaluation and optimization of $LiNO_3$-KNO_3-$NaNO_3$ ternary system. Calphad 2020; 71: 102202. https://doi.org/10.1016/j.calphad.2020.102202.
35. Zhong Y, Wang M, Yuan JS. Thermodynamic description of the quaternary $Mg(NO_3)_2$-KNO_3-$NaNO_3$-$LiNO_3$ system and investigation on the novel $Mg(NO_3)_2$ based nitrate salts with low temperature. Sol Energy Mater Sol Cells 2021; 230: 111148. https://doi.org/10.1016/j.solmat.2021.111148.

36. Han DM, Lougou BG, Shuai Y, Wang W, Jiang BS, Shagdar E. Study on thermophysical properties of solar salt composites doped with nanoparticles. Sol Energy Mater Sol Cells 2022; 234: 111432. https://doi.org/10.1016/j.solmat.2021.111432.
37. Zhong Y, Yuan JS, Wang M, et al. Phase diagrams of binary systems $Mg(NO_3)_2$-KNO_3, $Mg(NO_3)_2$-$LiNO_3$ and ternary system $Mg(NO_3)_2$-$LiNO_3$-$NaNO_3$. J Chem Eng Data 2020; 65: 3420–3427. https://doi.org/10.1021/acs.jced.9b01091.
38. Zhang Y, Wang M, Li JL, Wang HY, Zhao YJ. Improving thermal energy storage and transfer performance in solar energy storage: Nanocomposite synthesized by dispersing nano boron nitride in solar salt. Sol Energy Mater Sol Cells 2021; 232: 111378. https://doi.org/10.1016/j.solmat.2021.111378.
39. Novikov AA, Dzuban AV, Kovalenko NA, Uspenskaya IA. Thermodynamic Properties and Phase Equilibria in the H_2O-$Ca(NO_3)_2$ System. J Chem Eng Data 2021; 66: 1839–1855. https://doi.org/10.1021/acs.jced.1c00102.
40. Lee J, Jo B. Surfactant-free synthesis protocol of robust and sustainable molten salt microcapsules for solar thermal energy storage. Sol Energy Mater Sol Cells 2021; 227: 110954. https://doi.org/10.1016/j.solmat.2020.110954.
41. Li JL, Zhang Y, Wang M. Novel high specific heat capacity ternary nitrate/nitrite eutectic salt for solar thermal energy storage. Sol Energy Mater Sol Cells 2021; 227: 111075. https://doi.org/10.1016/j.solmat.2021.111075.
42. Ji W, Cheng XM, Chen HX, Li L, Li YY, Liu Z. Efficient synthesis of regular spherical GO/SiO_2@Solar Salt microcapsules to enhance heat-storage capacity and cycle stability. Energy Convers Manage 2021; 245: 114637. https://doi.org/10.1016/j.enconman.2021.114637.
43. Wang T, Mantha D, Reddy RG. Thermodynamic properties of $LiNO_3$-$NaNO_3$-KNO_3-$2KNO_3$·$Mg(NO_3)_2$ system. Thermochim Acta 2013; 551: 92–98. https://doi.org/10.1016/j.tca.2012.09.035.
44. Zhang HT, Zhao YJ, Shi LJ, Kang WQ, Wang M. Preparation and Thermal Properties of High-purified Molten Nitrate Salt Materials with Heat Transfer and Storage. High Temp Mater Processes 2015; 34: 839–846. https://doi.org/10.1515/htmp-2014-0147.
45. Zhang HT, Zhao YJ, Shi LJ, Kang WQ, Wang M. Preparation and heat transfer and thermal storage properties of high-temperature molten nitrate salt. Mater Sci Forum 2015; 814: 60–64. https://doi.org/10.4028/www.scientific.net/MSF.814.60.

Figures

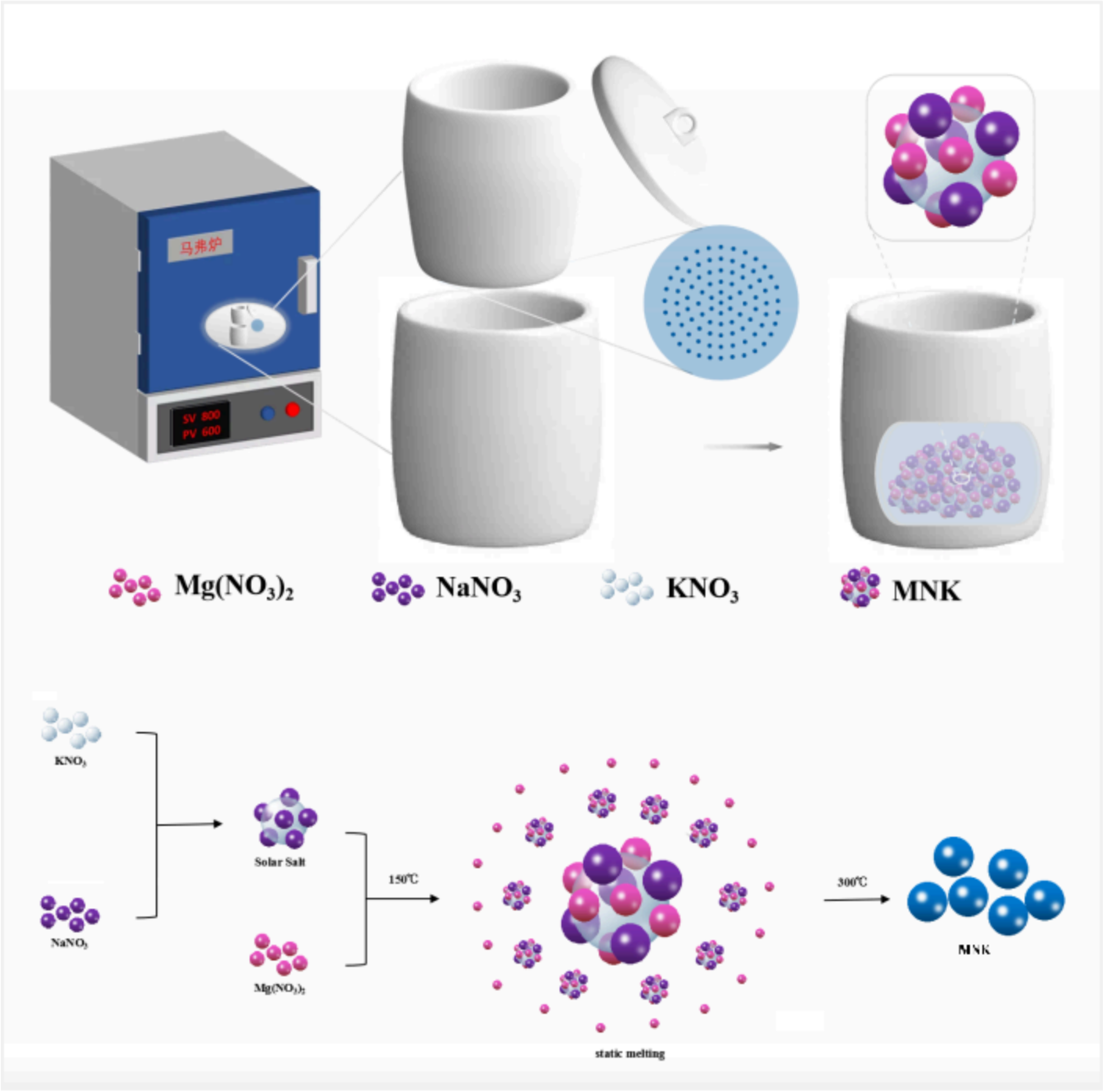


Figure 1

The schematic diagram of mixed molten salt.

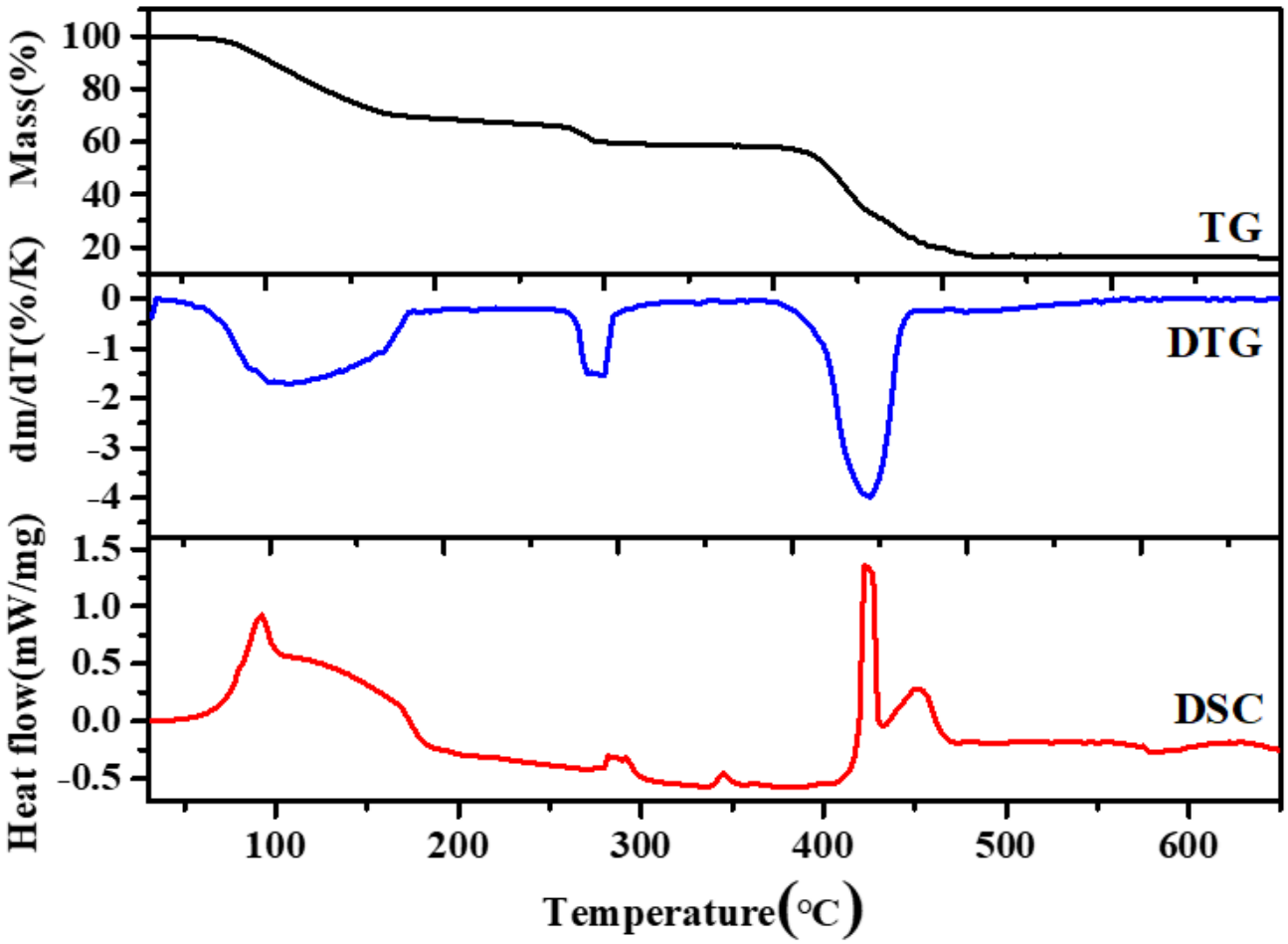


Figure 2

TG, DTG and DSC curves of $Mg(NO_3)_2 \cdot 6H_2O$ thermal decomposition in a nitrogen atmosphere at 10 °C·min^{-1}.

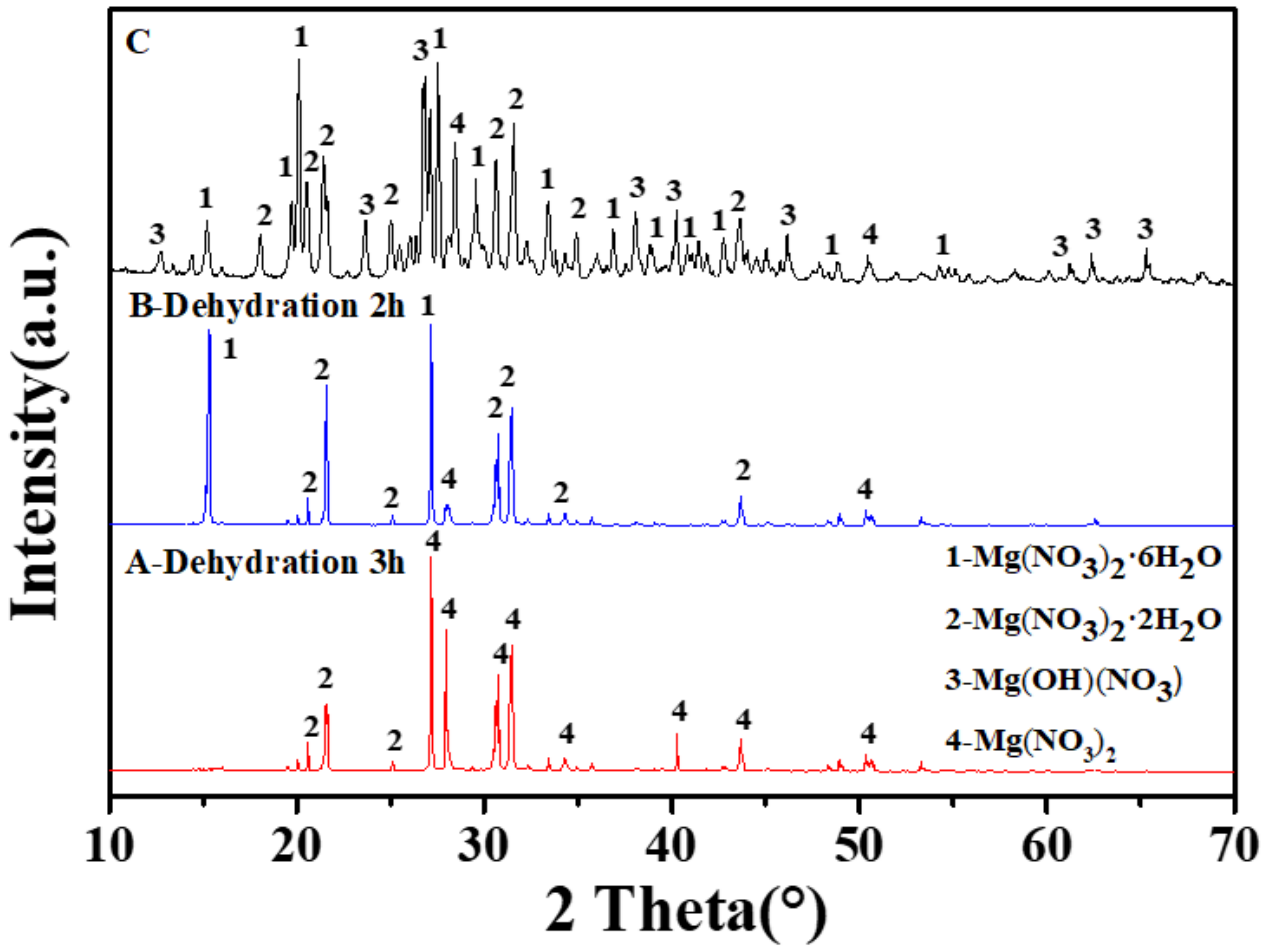


Figure 3

XRD pattern of dehydration $Mg(NO_3)_2{\cdot}6H_2O$ by different heat treatments and dehydration.

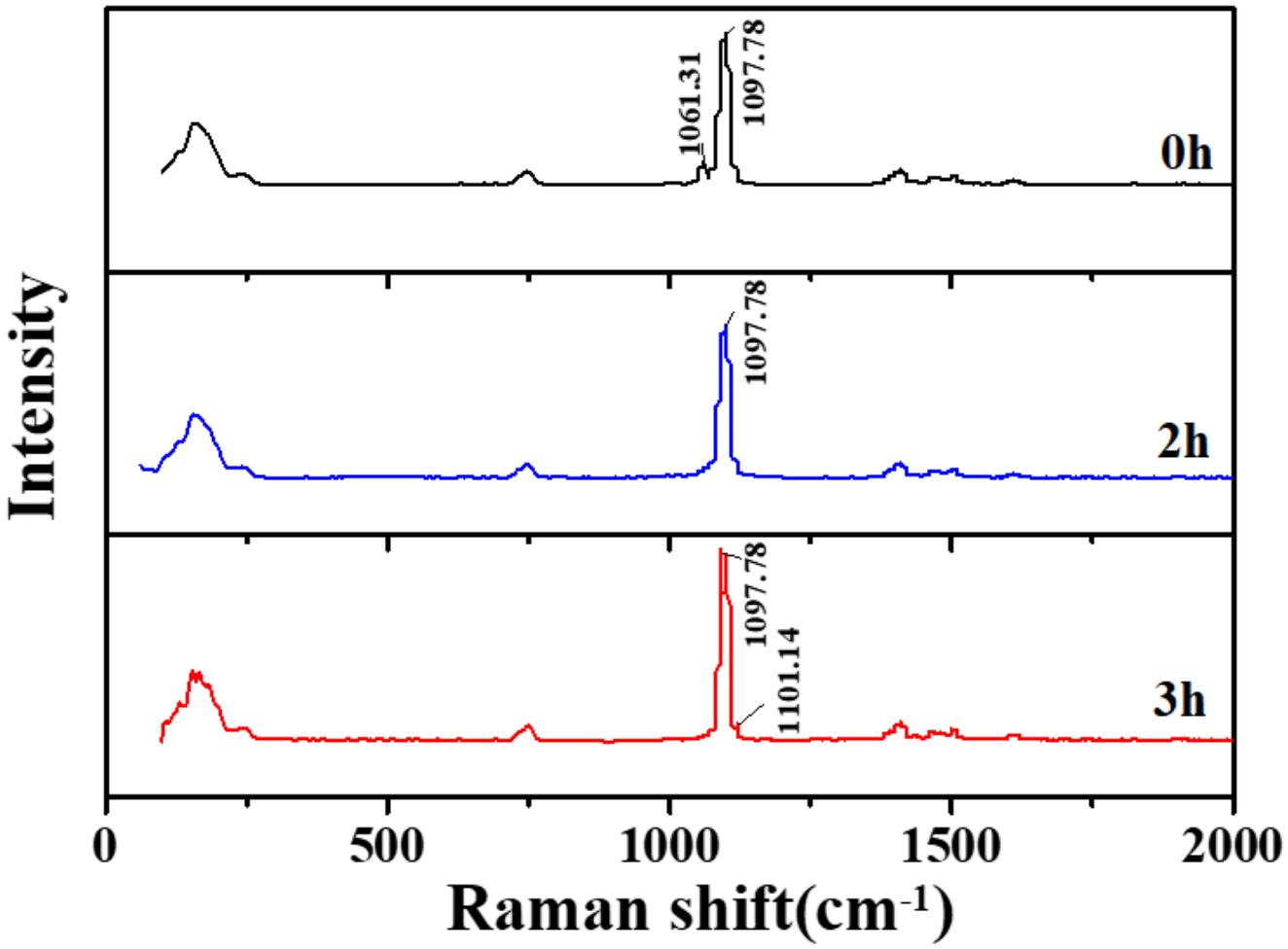


Figure 4

The Raman spectrum sample by different heat treatments and dehydration.

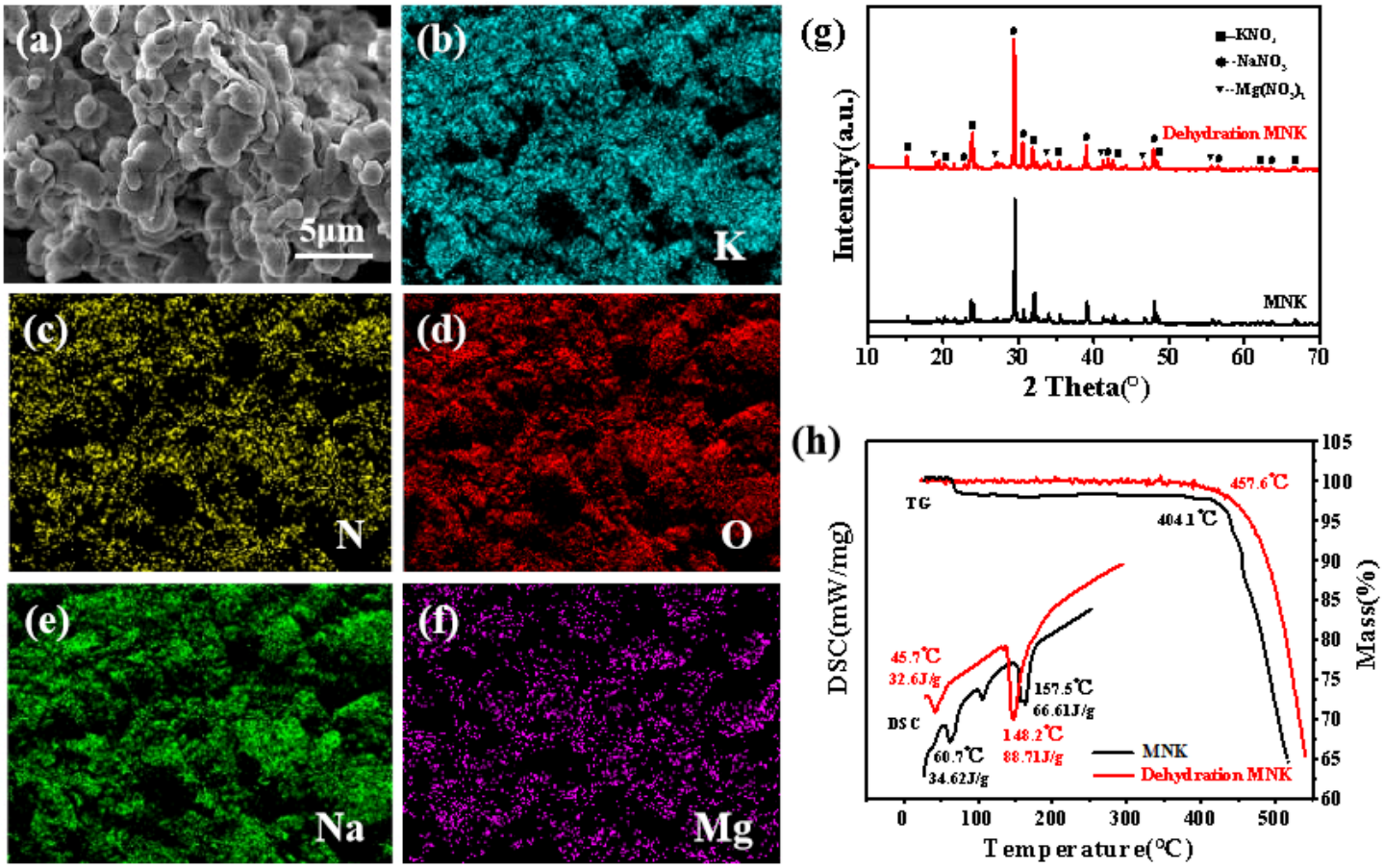


Figure 5

A lower magnification cross-sectional SEM image of the dehydration MNK ternary molten salt (a) and the corresponding EDX elemental maps (b-f); (g) XRD patterns of sample; (h) The TG-DSC results of sample.

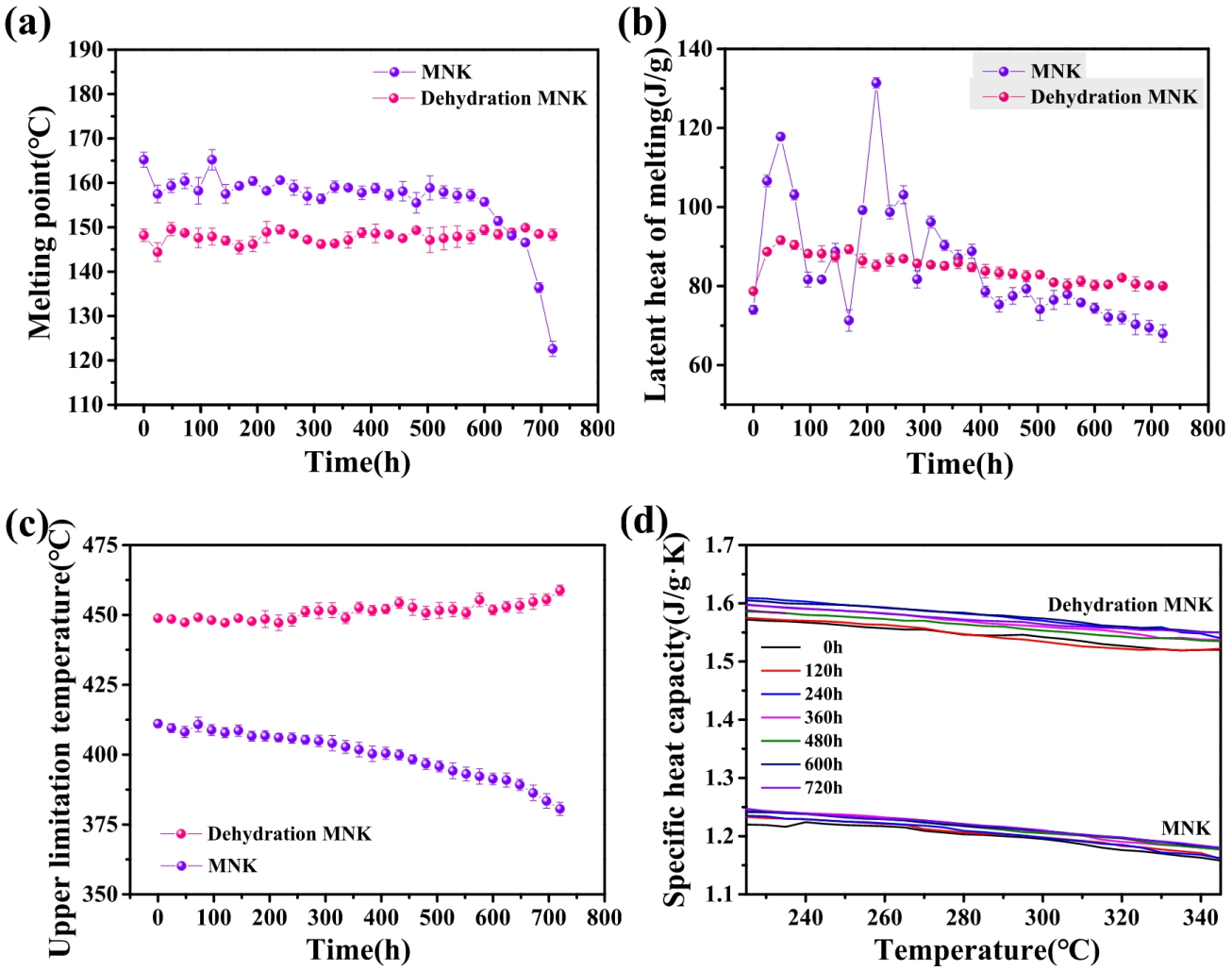


Figure 6

Thermal storage performance and cyclic durability of the MNK ternary molten salts. Melting point (a) , phase change enthalpy (b) and decomposition temperature (c) stability during 720 h of thermal cycling between 25 and 300 °C. (d) The specific heat capacity of the dehydrated sample during the 720 h test.

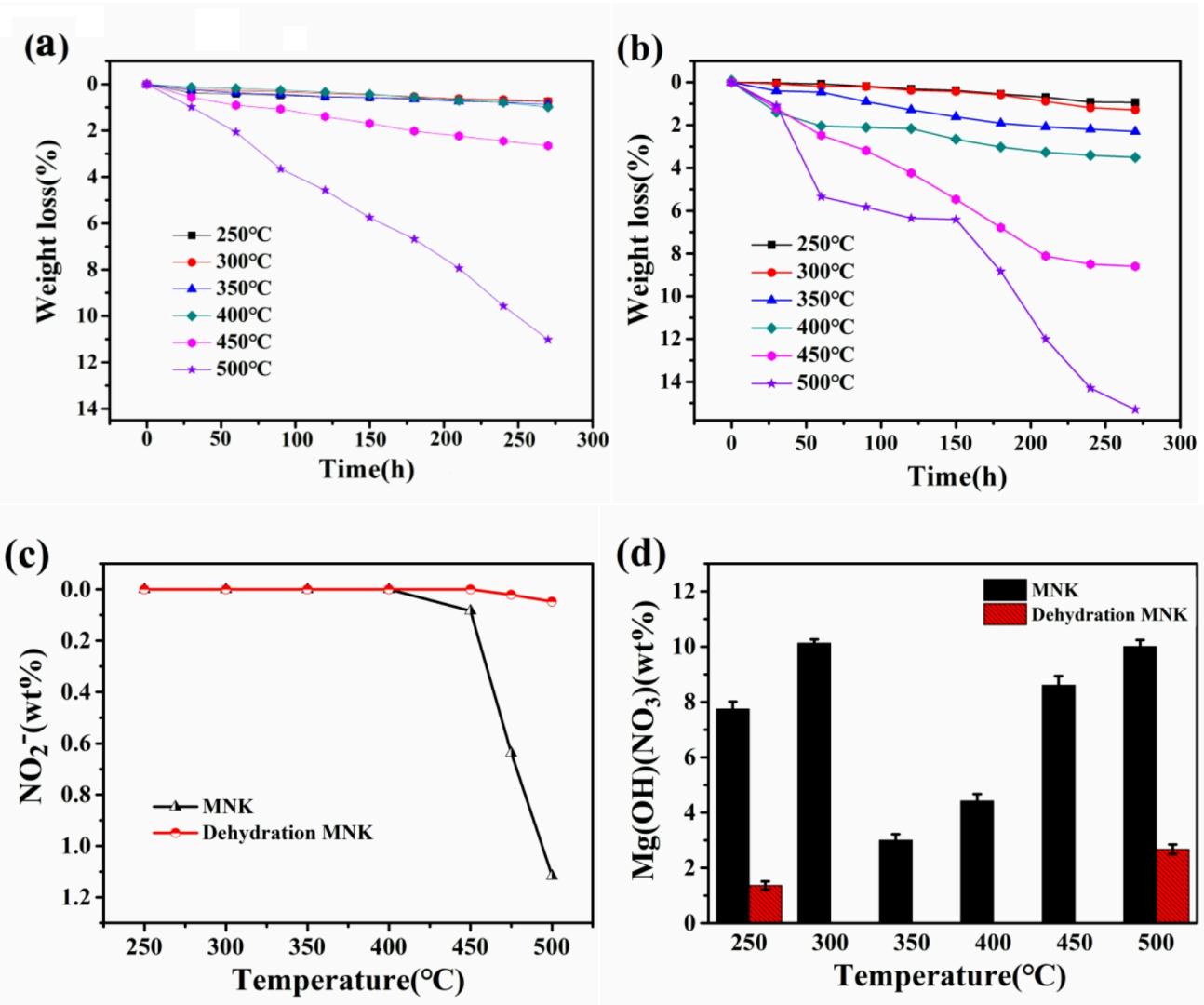


Figure 7

Weight loss vs. time of MNK molten salt at different temperature: (a)Dehydration MNK; (b)MNK; (c,d)The quantity of NO_2^- and $Mg(OH)(NO_3)$ in the MNK molten salt at different temperatures after ten cycles.